Phase Vector Incompressible Registration Algorithm (PVIRA) for Motion Estimation from Tagged Magnetic Resonance Images

Fangxu Xing*, Jonghye Woo, *Member, IEEE,* Arnold D. Gomez, Dzung L. Pham, *Member, IEEE,* Philip V. Bayly, Maureen Stone, and Jerry L. Prince, *Fellow, IEEE*

***Abstract*—Tagged magnetic resonance imaging has been used for decades to observe and quantify motion and strain of deforming tissue. It is challenging to obtain three-dimensional (3D) motion estimates due to a tradeoff between image slice density and acquisition time. Typically, interpolation methods are used to either combine two-dimensional motion extracted from sparse slice acquisitions into 3D motion, or construct a dense volume from sparse acquisitions before image registration methods are applied. This paper proposes a new phase-based 3D motion estimation technique that first computes harmonic phase volumes from interpolated tagged slices and then matches them using an image registration framework. The approach uses several concepts from diffeomorphic registration with a key novelty that defines a symmetric similarity metric on harmonic phase volumes from multiple orientations. The material property of harmonic phase solves the aperture problem in optical flow and intensity-based methods. A harmonic magnitude volume is used in enforcing incompressibility in the tissue region. The estimated motion fields are dense, incompressible, diffeomorphic, and inverse-consistent at a 3D voxel level. The method was evaluated using simulated phantoms, human brain data in mild head accelerations, human tongue data during speech, and an open cardiac dataset. The method shows comparable accuracy to three existing methods, while demonstrating major advantages in preventing tag fading, increasing noise robustness, reducing processing complexity, and improving computation speed.**

***Index Terms*—Motion, 3D, tagged MRI, phase, registration, incompressible.**

I. Introduction

THE analysis of biological motion using medical imaging techniques has been an important topic of research for both clinical and scientific purposes. Its application ranges from cardiac imaging [1], [2] to studies in speech and swallowing [3] to analysis of brain motion in traumatic injuries [4], [5], etc. Tagged magnetic resonance (MR) imaging is a widely used technique for quantifying soft tissue motion [6], [7]. It places temporary markers (tags) in the tissue of interest that move and deform together with tissue during motion. Many methods for estimating two-dimensional (2D) tissue motion and strain from the deformed tag patterns have been proposed in the past, including tag line tracking [8], [9], tag intersection tracking [10]–[12], and pixel-wise tracking using harmonic phase or Gabor filters [13]–[16] etc.

While measuring 2D motion alone might be sufficient in some applications, knowledge of three-dimensional (3D) motion is necessary or highly desirable in others. Methods to measure 3D motion from densely-acquired tagged MR images have been proposed in the past. They require an acqusition of a large number of closely spaced image slices, which is equivalent to direct acquisition of a dense 3D volume. In this case, traditional 2D methods can be extended to 3D and directly applied to compute the dense motion [17]–[20]. However, the large amount of time that it takes to acquire these images makes this approach impractical for routine clinical or scientific use. For this reason, most of the reported 3D motion estimation methods have been focused on the use of sparse collections of 2D images and 2D motion estimation followed by interpolation in order to achieve 3D motion estimation.

Fig. 1 shows a typical imaging geometry for a sparse acquisition of tagged MR images of the brain during mild acceleration [5]. The slices are taken to cover the whole brain but due to time constraints the slice spacing is large. In each axial image plane, two sets of images are taken in the same location, one with horizontal tags and the other with vertical tags. In this way, the motion in the x and y directions can be observed in these two sets. In order to record the z motion, sagittal slices with horizontal tags are also acquired. For each slice position, MR tags are placed at a reference time and a sequence of images are acquired over time in order to reveal the motion as a deforming tag pattern. Because of the acquisition geometry, the available motion data are sparse in the through-plane direction. Similar geometries are used in both cardiac and speech studies. As a result, motion features that are observed in the acquired image planes must be interpolated in some way in order to observe dense 3D motion.

Incompressibility is an important consideration in the estimation of biological motions. For example, during a cardiac cycle, the change in volume of the myocardium is less than

Manuscript received June 1, 2016. This work was supported by NIH/NIDCD 1R01DC014717 and NIH/NINDS 4R01NS055951. *Asterisk indicates corresponding author.*

*F. Xing is with the Department of Radiology, Massachusetts General Hospital/Harvard Medical School, Boston, MA, 02114 USA (e-mail: fxing1@mgh.harvard.edu).

J. Woo is with the Department of Radiology, Massachusetts General Hospital/Harvard Medical School, Boston, MA, 02114 USA.

A. D. Gomez and J. L. Prince are with the Department of Electrical and Computer Engineering, Johns Hopkins University, Baltimore, MD, 21218 USA.

D. L. Pham are with the Center for Neuroscience and Regenerative Medicine, The Henry M. Jackson Foundation, Bethesda, MD, 20817 USA.

P. V. Bayly is with the Department of Mechanical Engineering and Materials Science, Washington University in St. Louis, St.Louis, MO, 63130 USA.

M. Stone is with the Department of Neural and Pain Sciences, University of Maryland School of Dentistry, Baltimore, MD, 21201 USA.

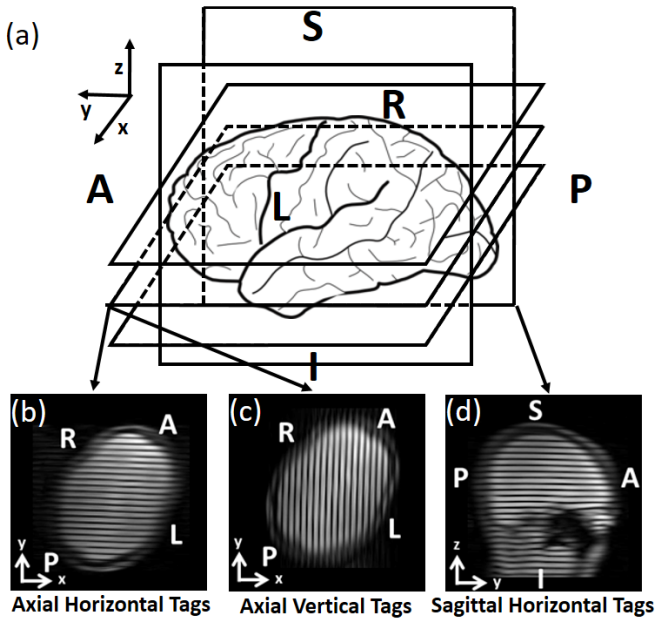

Fig. 1: Illustration of the acquisition locations of tagged MR image slices for 3D motion. A: anterior. P: posterior. L: left. R: right. S: superior. I: inferior.

4% [21], [22], and the change in volume of the tongue during speech and swallowing is even smaller [23]. Therefore, the motion of muscles can be assumed to be incompressible [24]. In the study of brain motion under mild accelerations, there is very little exchange of fluid in the ventricular system and the total brain volume including the ventricles remains very nearly constant [5]. Therefore, incompressibility can also be assumed in studies of small brain motions under mild accelerations created inside an MR scanner. In summary, motion estimation in many organs requires the final dense estimated motion field to be incompressible in order to represent the tissue's true physical property.

Previous works on 3D motion estimation from sparse imaging geometries are quite varied. Some use finite element or finite difference methods [25], [26], some use tag line tracking based on 2D images [27], [28], some use spline interpolation [27], [29]–[32], some use the organ's biomechanical properties [33], [34], and some are based on harmonic phase tracking [31], [35]. More methods are summarized in the collected works of [36]. A common limitation of these methods is the problem of over-complexity. Because the computations are typically limited to the organ of interest, a 3D segmentation method is commonly required [25], [27], [29], [37]; this step requires either human intervention or automated segmentation algorithms [38] that increase the demand on processing time. Moreover, in order to incorporate incompressibility, because of the assumption of sparse imaging geometry, previous methods have been of the interpolation variety. The methods in [39], [40] use divergence-free radial basis functions while the methods in [31], [41] use smoothing vector splines seeking a divergence-free velocity field that yield a nearly incompressible deformation field when integrated. Unfortunately, vector interpolation further increases processing complexity of these methods, causing even days of processing time for one subject with many temporal volumes.

On the other hand, in recent developments, intensity-based methods have gradually become the major focus of tagged motion estimation [42]–[47]. These methods directly aim at matching intensity values between tagged voxels using optical flow assumptions, and are straightforward to incorporate additional desired properties. For example, extension of these methods to focus on 3D motion estimation has been proposed in [48]–[53]. The method in [54] directly tackles sparse acquisition problem. There are also methods that addresses incompressibility such as [55]. Specifically, image registration algorithms based on dense imaging geometries can accommodate incompressibility in various ways. For example, the widely-adapted diffeomorphic demons algorithm [56] has been extended to include volume-preserving deformations [57], [58] and applied to tagged intensity data. However, the common premise of intensity-based methods—matching of intensity values—is not robust to intensity variation and degeneration [59]. Higher noise can easily affect their performance. Also, tags are known to fade in later time frames with the T_1 constant of the tissue. Previous experiments have shown failure of intensity matching under tag fading [60]. Since phase values are relative positions of the underlying sinusoidal pattern and reflect the material property of the tissue, the use of phase is preferred to counter these effects. There has been recent work [61] on phase-based motion estimation, but properties such as incompressibility were not incorporated. Despite the number and diversity of previous approaches, there does not yet exist a straightforward and highly effective phase-based algorithm for estimating dense incompressible motions from the sparse imaging geometries of tagged MRI.

In this paper, we propose a new phase-based method to tackle this problem. The method first interpolates raw tagged images onto a denser grid and then applies the harmonic phase (HARP) method [14] to yield 3D harmonic phase volumes. We use these volumes in a multichannel image registration algorithm to track tissue points over time. The image registration algorithm is based on iLogDemons [58], but contains several key differences. First, to drive the registration process, we use a new symmetric harmonic phase vector similarity metric. Second, to compensate for harmonic phase wrapping, we incorporate a special phase interpolation method. Finally, to enforce incompressibility only within tissue regions, we use the harmonic magnitude image along with the divergence-free velocity constaint of iLogDemons. We call the proposed method PVIRA, which stands for *Phase Vector Incompressible Registration Algorithm*. PVIRA was evaluated using simulation, MR data from the human brain in rotation, the human tongue in speech, and an open cardiac dataset [62]. We compared its result against three methods: 3D HARP tracking, IDEA [31], and direct intensity registration. The evaluations show better robustness to noise and tag fading and a major reduction in computation complexity. PVIRA is demonstrated to yield a nearly incompressible result and to produce motion and inverse motion fields that are very nearly inverse-consistent.

This paper is organized as follows. Section II.A discusses

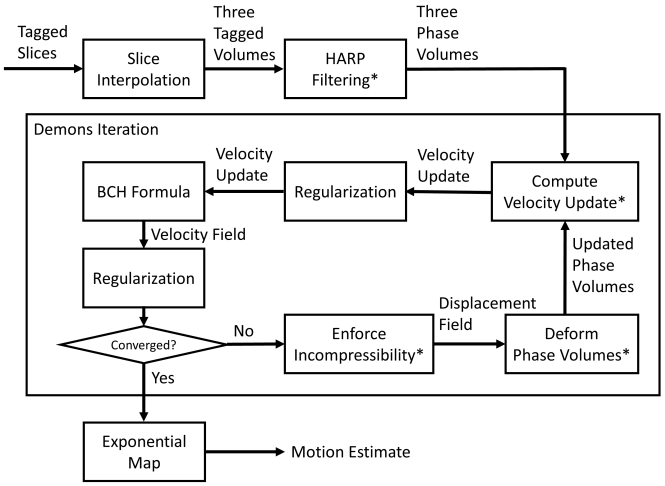

Fig. 2: Flow chart of the proposed method PVIRA. Asterisks indicate steps involving special harmonic phase and magnitude operations.

the interpolation of tagged slices. Section II.B presents the HARP method and the production of phase volumes. Section II.C briefly introduces the iLogDemons method and Section II.D presents the new similarity metric used to drive the velocity update process in PVIRA. Section II.E discusses the interpolation and deformation of phase volumes and Section II.F shows how incompressibility is incorporated. Section III shows the experimental results on simulation and real data. Section IV discusses the method and Section V concludes the paper.

II. Methods

The complete work flow of PVIRA is shown in Fig. 2. Sparse tagged slices are processed with interpolation and HARP filtering before the demons iteration loop for motion estimation. Below we explain each step in detail.

A. Interpolation of Tagged Slices

We use tricubic b-spline interpolation [63] to produce an arbitrarily dense 3D tagged volume with isotropic resolution, as illustrated in Fig. 3. In this scenario, we let $\mathbf{x}_s \in \mathcal{Z}$ denote the location from the set of points sampled by the sparsely acquired sagittal slices $I_a(\mathbf{x}_s)$ having horizontal tag planes. These locations are shown as blue dots in Fig. 3(a). Since horizontal tag planes in a sagittal acquisition are oriented in the axial direction, subscript a is used in the notation I_a. We denote points in the dense 3D grid by $\mathbf{x}$, as shown using red dots in Fig. 3(a). Tricubic b-spline interpolation then finds the values $I_a(\mathbf{x})$ by

$$I_a(\mathbf{x}) = \sum_{\mathbf{x}_s \in \mathcal{Z}} c(\mathbf{x}_s)\beta^3(\mathbf{x} - \mathbf{x}_s), \tag{1}$$

where $\beta^3(\mathbf{x})$ is the cubic b-spline interpolation kernel and $c(\mathbf{x}_s)$ are the interpolation coefficients computed from $I_a(\mathbf{x}_s)$ [64]. Four interpolated saggital slices zoomed in on the tongue region are shown in Fig. 3(c). In a similar fashion,

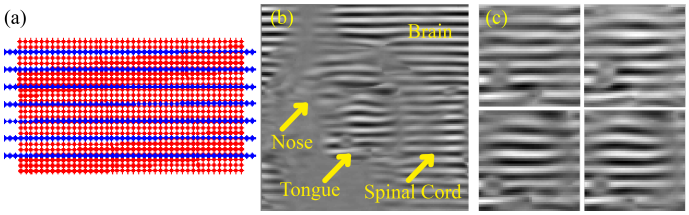

Fig. 3: Demonstration of interpolation of tagged slices on tagged images of the tongue. (a) Spatial locations of acquired samples (blue) and interpolated samples (red). (b) A tagged sagittal tongue slice from acquisition. (c) Four interpolated sagittal tongue slices with horizontal tags.

the two axial acquisitions (see Fig. 1) containing horizontal and vertical tags can be interpolated onto the same 3D grid to create the image $I_c(\mathbf{x})$ having coronal tag planes and the image $I_s(\mathbf{x})$ having sagittal tag planes. The output of interpolation is a dense 3D volume in which each voxel has samples of three tagged volumes where the tags (prior to motion) are oriented in the three cardinal directions. This process is repeated at each time frame, yielding a sequence of such vectorized tagged volumes. Note that we pick an interpolated resolution same as the acquired in-plane resolution, because it would be imprudent to reduce the in-plane resolution to a worse resolution than original, and a finer resolution would be equally imprudent since that would increase computation time with no improvement in underlying resolution.

B. Harmonic Phase Volumes

The HARP algorithm [14] is a benchmark phase-based method to process tagged MR images. In this method, one of the major harmonic peaks in the Fourier domain of a tagged image slice is bandpass filtered (so-called HARP filtering) to yield a complex-valued image (see Fig. 4) where motion information is contained in the phase part (HARP phase) and anatomical information is contained in the magnitude part (HARP magnitude). While originally developed to analyze 2D images, the HARP framework is valid in 3D and has been previously used by Ryf et al. [17] to carry out 3D HARP tracking to compute displacement fields from densely acquired tagged images. We refer to this method as 3D HARP.

Following this strategy, our method performs HARP filtering on the three interpolated tagged volumes I_a, I_c, and I_s. For example, for the volume $I_a(\mathbf{x})$, the complex image after HARP filtering can be denoted as

$$J_a(\mathbf{x}) = M_a(\mathbf{x})e^{j\Phi_a(\mathbf{x})}, \tag{2}$$

where $M_a(\mathbf{x})$ is the HARP magnitude volume and $\Phi_a(\mathbf{x})$ is the HARP phase volume. The same notation applies for coronally and sagittally tagged volumes, yielding $J_c(\mathbf{x})$, $M_c(\mathbf{x})$, $\Phi_c(\mathbf{x})$, $J_s(\mathbf{x})$, $M_s(\mathbf{x})$, and $\Phi_s(\mathbf{x})$.

C. iLogDemons

The registration framework of iLogDemons [58] is used as the major structure for PVIRA. Summarized in Algorithm 1,

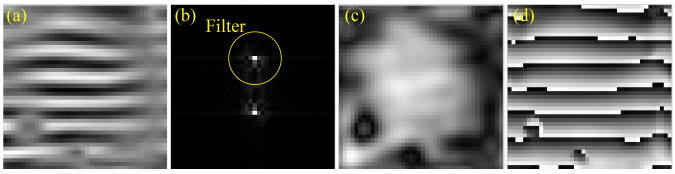

Fig. 4: HARP processing of a tagged image. (a) A tagged slice. (b) Harmonic peaks in the Fourier domain. (c) Harmonic magnitude slice. (d) Harmonic phase slice.

iLogDemons is an iterative method alternating between force-driven stepwise update and deformation field regularization. Its result is an invertible motion field and incompressibility is applied in the process. Suppose $I_0(\mathbf{x})$ is a fixed intensity image and $I_t(\mathbf{x})$ is a moving image, by minimizing the demon energy $||I_0(\mathbf{x}) - I_t \circ \exp(\mathbf{v}(\mathbf{x}))||^2 + K||\nabla \mathbf{v}(\mathbf{x})||^2$, an optimal update velocity field $\delta\mathbf{v}(\mathbf{x})$ can be found. From [65], the symmetric form of $\delta\mathbf{v}(\mathbf{x})$ is given by

$$\delta\mathbf{v}(\mathbf{x}) = \frac{2(I_0(\mathbf{x}) - I'_t(\mathbf{x}))(\nabla I_0(\mathbf{x}) + \nabla I'_t(\mathbf{x}))}{||\nabla I_0(\mathbf{x}) + \nabla I'_t(\mathbf{x})||^2 + K(I_0(\mathbf{x}) - I'_t(\mathbf{x}))^2}\,, \quad (3)$$

where $I'_t(\mathbf{x}) = I_t \circ \psi(\mathbf{x})$ is the moving image deformed with the current motion estimate ψ, and K is a normalization factor. Note that the motion estimate $\psi(\mathbf{x}) = \exp(\mathbf{v}(\mathbf{x}))$ uses the exponential map of a stationary velocity estimate $\mathbf{v}(\mathbf{x})$, which is the main quantity that must be estimated in the "log domain".

Algorithm 1. iLogDemons Registration Algorithm

1. Set the initial velocity estimate $\mathbf{v}(\mathbf{x})$ to zero.
2. Compute the update velocity $\delta\mathbf{v}(\mathbf{x})$ using Eqn. (3).
3. Regularize $\delta\mathbf{v}(\mathbf{x})$ with a Gaussian kernel.
4. Compose $\mathbf{v}(\mathbf{x})$ with $\delta\mathbf{v}(\mathbf{x})$ using the BCH formula [58] and set the result to be the new velocity estimate $\mathbf{v}(\mathbf{x})$.
5. Regularize $\mathbf{v}(\mathbf{x})$ with a Gaussian kernel.
6. Restrict incompressibility by solving Poisson's equation $\nabla^2 p = \nabla \cdot \mathbf{v}(\mathbf{x})$ and setting $\mathbf{v}(\mathbf{x}) - \nabla p$ as the new $\mathbf{v}(\mathbf{x})$.
7. Deform $I_t(\mathbf{x})$ with $\exp(\mathbf{v}(\mathbf{x}))$ to create a new moving image $I'_t(\mathbf{x})$.
8. Go to Step 2. Repeat until convergence.
9. The motion estimate is $\psi(\mathbf{x}) = \exp(\mathbf{v}(\mathbf{x}))$ and the inverse motion estimate is $\psi^{-1}(\mathbf{x}) = \exp(-\mathbf{v}(\mathbf{x}))$.

D. Registration of Phase Volumes

A HARP phase value $\Phi(\mathbf{x})$ is in fact a true phase value $\Theta(\mathbf{x})$ wrapped into the range of $[-\pi, \pi)$, i.e.,

$$\Phi(\mathbf{x}) = W(\Theta(\mathbf{x}))\,, \quad (4)$$

where

$$W(\Theta) = \mathrm{mod}(\Theta + \pi, 2\pi) - \pi\,. \quad (5)$$

This is illustrated in Fig. 5. Since iLogDemons works only with intensity images, its framework needs to be modified to adapt to wrapped phase. Although phase unwrapping [66]–[68] could potentially recover the true phase, it is known that 3D phase unwrapping is problematic [69]. Therefore, rather than attempting to carry out global phase unwrapping, we reformulate the required mathematical operations as follows.

The first operation is the calculation of phase difference, for which we define a new "asterisked subtraction" operator $-^*$. Consider two wrapped phases $\Phi_1 = W(\Theta_1)$ and $\Phi_2 = W(\Theta_2)$. If the underlying true phases satisfy the condition $|\Theta_1 - \Theta_2| < \pi$, then

$$\Theta_1 - \Theta_2 = \Phi_1 -^* \Phi_2 = W(\Phi_1 - \Phi_2)\,. \quad (6)$$

This implies that carrying out subtraction on observed harmonic phases followed by an explicit re-wrapping will recover the true phase difference if it is small enough. This condition is satisfied in tissue motion when the tags do not deform more than half a period, a condition that normally holds for tagged MR acquisitions in the brain, tongue, and heart. We call this a *small motion condition*. This is an assumption commonly used in phase-based methods.

The second operation is the calculation of spatial gradient. The true gradient can be rigorously recovered from the wrapped gradient with a mathematical trick denoted as a "asterisked gradient" ∇^* [14]:

$$\begin{aligned}\nabla\Theta(\mathbf{x}) &= \nabla^*\Phi(\mathbf{x}) \\ &= \begin{cases} \nabla\Phi(\mathbf{x}), & \text{if } |\nabla\Phi(\mathbf{x})| \le |\nabla W(\Phi(\mathbf{x}) + \pi)|\,, \\ \nabla W(\Phi(\mathbf{x}) + \pi), & \text{otherwise.} \end{cases}\end{aligned} \quad (7)$$

This procedure computes gradients on both the original phase function and on the phase that has been shifted by π and then re-wrapped. The correct gradient is the one with smaller magnitude.

For the three pairs of HARP phase volumes, we redefine the demons energy as

$$\begin{aligned}E_t(\mathbf{v}) = &||\Phi_{a0}(\mathbf{x}) - \Phi_{at} \circ \psi(\mathbf{x})||^2 + ||\Phi_{c0}(\mathbf{x}) - \Phi_{ct} \circ \psi(\mathbf{x})||^2 \\ &+ ||\Phi_{s0}(\mathbf{x}) - \Phi_{st} \circ \psi(\mathbf{x})||^2 + K||\nabla\mathbf{v}||^2,\end{aligned} \quad (8)$$

where the subscripts 0 and t denote time frame number. Note that the 0 subscript is only used to indicate a reference time frame. It can be any previous time point, not necessarily the very first one. Also note that all three pairs of phase volumes with three tag directions are used simultaneously because each pair provides a main motion component in the x, y, and z directions, and we give equal weights to each because they contribute equally. We follow an analogous strategy as that in [56] to find the $\mathbf{v}(\mathbf{x})$ that minimizes E_t. It yields the proposed

update velocity field in the demons framework:

$$\begin{aligned}
\delta\mathbf{v}(\mathbf{x}) &= 2\boldsymbol{\alpha}_0(\mathbf{x})/(\alpha_1(\mathbf{x}) + \alpha_2(\mathbf{x})/K)\ , \text{where} \\
\boldsymbol{\alpha}_0(\mathbf{x}) &= (\Phi_{a0}(\mathbf{x}) -^* \Phi'_{at}(\mathbf{x}))(\nabla^*\Phi_{a0}(\mathbf{x}) + \nabla^*\Phi'_{at}(\mathbf{x})) \\
&\quad + (\Phi_{s0}(\mathbf{x}) -^* \Phi'_{st}(\mathbf{x}))(\nabla^*\Phi_{s0}(\mathbf{x}) + \nabla^*\Phi'_{st}(\mathbf{x})) \\
&\quad + (\Phi_{c0}(\mathbf{x}) -^* \Phi'_{ct}(\mathbf{x}))(\nabla^*\Phi_{c0}(\mathbf{x}) + \nabla^*\Phi'_{ct}(\mathbf{x}))\ , \\
\alpha_1(\mathbf{x}) &= ||\nabla^*\Phi_{a0}(\mathbf{x}) + \nabla^*\Phi'_{at}(\mathbf{x})||^2 \\
&\quad + ||\nabla^*\Phi_{s0}(\mathbf{x}) + \nabla^*\Phi'_{st}(\mathbf{x})||^2 \\
&\quad + ||\nabla^*\Phi_{c0}(\mathbf{x}) + \nabla^*\Phi'_{ct}(\mathbf{x})||^2\ , \\
\alpha_2(\mathbf{x}) &= (\Phi_{a0}(\mathbf{x}) -^* \Phi'_{at}(\mathbf{x}))^2 + (\Phi_{s0}(\mathbf{x}) -^* \Phi'_{st}(\mathbf{x}))^2 \\
&\quad + (\Phi_{c0}(\mathbf{x}) -^* \Phi'_{ct}(\mathbf{x}))^2\ .
\end{aligned} \tag{9}$$

Note that Φ'_{at}, Φ'_{st}, and Φ'_{ct} are Φ_{at}, Φ_{st}, and Φ_{ct} deformed with current ψ (see next section). The metric used is similar to previous multi-channel image registration metrics [70], but is specifically adapted to HARP phase. In particular, the difference and gradient operations have been modified to deal with phase wrapping.

E. Deformation of Phase Volumes

Now we discuss the deformation of Φ_{at}, Φ_{st}, and Φ_{ct} using the current motion estimate $\psi(\mathbf{x})$ at each demons iteration step. Since interpolation is used to find sub-voxel values of the deformed phase, the effect of phase wrapping must also be considered. As illustrated in Fig. 5 for a one-dimensional example, suppose the phase value at sub-voxel location x_0 needs to be found from the known phases $\Phi(x_1)$ and $\Phi(x_2)$ at two neighbor voxels x_1 and x_2. Linear interpolation would give $\hat{\Phi}(x_0) = (\Phi(x_2) - \Phi(x_1))(x_0 - x_1)/(x_2 - x_1)$. In this case the value $\hat{\Phi}(x_0)$ equals the real phase $\Theta(x_0)$ because no wrapping is involved. The situation is different at location y_0, however. In this case, since $\Phi(y_2)$ has been wrapped from the true value $\Theta(y_2)$, $(\Phi(y_2) - \Phi(y_1))(y_0 - y_1)/(y_2 - y_1)$ yields the wrong result, while the correct value is computed by unwrapping $\Phi(y_2)$ to $\Phi(y_2) + 2\pi$.

To provide a correct phase interpolation we first note that $(\Phi(y_2) + 2\pi) - \Phi(y_1) = W(\Phi(y_2) - \Phi(y_1))$. Whenever an abnormal phase difference greater than 2π is caused by wrapping, under the small motion condition (see previous section), the abnormal difference must be a jump of $\pm 2\pi$. Because of this fact, the error can be removed by re-wrapping the phase difference. Therefore, when deforming phase volumes and using interpolation in each of the three x, y, and z directions, every phase subtraction must be computed with wrapping, i.e.,

$$\hat{\Phi}(y_0) = W(\frac{y_0 - y_1}{y_2 - y_1} \cdot (\Phi(y_2) -^* \Phi(y_1)))\ . \tag{10}$$

F. Incorporation of Incompressibility

In iLogDemons [58], incompressibility is enforced at every iteration by computing the "divergence part" of the velocity and removing it, i.e., solve Poisson's equation $\nabla^2 p = \nabla \cdot \mathbf{v}(\mathbf{x})$ to find the conservative (curl-free) part $\mathbf{v}_d(\mathbf{x}) = \nabla p$ and update the velocity by $\mathbf{v}(\mathbf{x}) - \mathbf{v}_d(\mathbf{x})$. In PVIRA, since only the tissue region is incompressible, we normalize the previously generated HARP magnitude volumes $M_a(\mathbf{x})$, $M_c(\mathbf{x})$, and

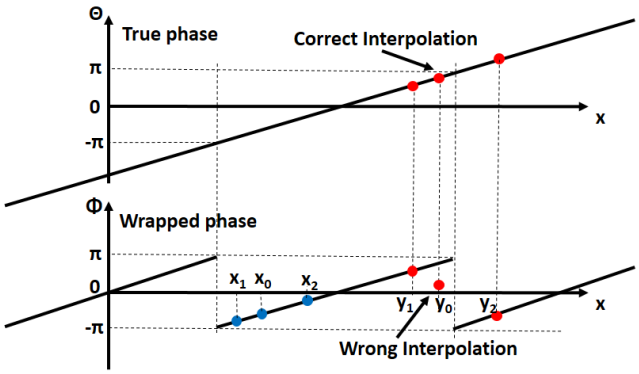

Fig. 5: Linear interpolation of wrapped phase values.

$M_s(\mathbf{x})$ to the range between [0,1] and use their mean $M(\mathbf{x})$ as a weighted mask to specify the region of incompressibility. The velocity is then updated according to Eqn. (11) which enforces incompressibility only in the tissue region where $M(\mathbf{x}) \approx 1$.

$$\mathbf{v}(\mathbf{x}) \longleftarrow \mathbf{v}(\mathbf{x}) - M(\mathbf{x})\mathbf{v}_d(\mathbf{x})\ . \tag{11}$$

Since HARP magnitude is computed simultaneously with HARP phase, this strategy removes the requirement of a manual or automated segmentation step, as is often required in other tag tracking approaches. Also, in the condition of tag fading, since the magnitude is normalized, unless the tags completely fade to zero, the incompressible constraint is not affected.

PVIRA is summarized in Algorithm 2. Novel steps comparing to iLogDemons are marked with asterisks.

III. Experiments and Results

A. Simulation of Brain and Tongue Deformation

Since true motion of human data is difficult to find, simulation is important to evaluate PVIRA's performance. In this first experiment, we simulated deformations of the brain in a rotation and the tongue in speech. Note that these simulations aimed to produce variations in the amount of displacement, motion type, tag condition, and noise level. The modeling of more realistic subject-specific biomechanical motions requires more complex techniques and is not the focus of this current work.

For the brain, a $64 \times 64 \times 64$ volume was generated with 1.0 mm voxel resolution and 10.0 mm tag period. To represent the gelatin phantom used in [5], the tissue exists on a cylinder-shaped region with a circular cross-section in the x-y plane and is isometric in the z direction. Synthetic displacement fields were generated by a finite element simulation (COMSOL v4.3, COMSOL Multiphysics, Burlington, MA) of a nearly-incompressible soft material (11.2 cm diameter, 18 cm long, Youngs modulus $E = 5000$, Poissons ratio $\nu = 0.49$). The outer boundary of the cylinder was subjected to a half-sinusoidal angular acceleration pulse. Simulated displacements were x-y in-plane rotations around the center, as shown in Fig. 6(a). This increasing rotation lasted for 18 time frames

Algorithm 2. Phase Vector Incompressible Registration Algorithm (PVIRA)

1*. Interpolate tagged images using Eqn. (1) to get three sets of tagged volumes.
2*. Apply HARP filtering using Eqn. (2) on every volume to get HARP phase and HARP magnitude volumes.
3. Set the initial velocity estimate $\mathbf{v}(\mathbf{x})$ to zero.
4*. Compute the update velocity $\delta\mathbf{v}(\mathbf{x})$ using Eqn. (9). Difference and gradient computations must follow Eqns. (6) and (7).
5. Regularize $\delta\mathbf{v}(\mathbf{x})$ with a Gaussian kernel.
6. Compose $\mathbf{v}(\mathbf{x})$ with $\delta\mathbf{v}(\mathbf{x})$ using the BCH formula and set it to be the new $\mathbf{v}(\mathbf{x})$.
7. Regularize $\mathbf{v}(\mathbf{x})$ with a Gaussian kernel.
8*. Enforce incompressibility using Eqn. (11).
9*. Deform Φ_{at}, Φ_{st}, and Φ_{ct} with $\exp(\mathbf{v}(\mathbf{x}))$ to compute a new Φ'_{at}, Φ'_{st}, and Φ'_{ct}. Sub-voxel interpolation must follow Eqn. (10).
10. Go to Step 4. Repeat until convergence.
11. The motion estimate is $\psi(\mathbf{x}) = \exp(\mathbf{v}(\mathbf{x}))$ and the inverse motion estimate is $\psi^{-1}(\mathbf{x}) = \exp(-\mathbf{v}(\mathbf{x}))$.

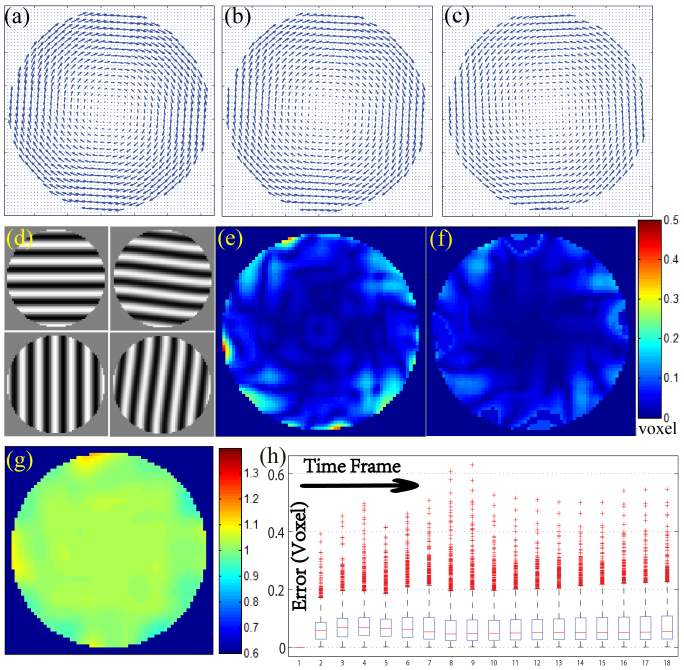

Fig. 6: Test of PVIRA on simulated brain rotations. (a) Simulated truth at time frame 10 (max displacement 2.8 mm). (b) Estimated motion. (c) Estimated inverse motion. (d) Simulated tags. (e) Magnitude of estimation error. (f) Inverse-consistency error. (g) Jacobian determinant of motion estimate. (h) Estimation error of all time frames. Center bar = median.

and yielded a 4.8 mm maximum displacement, satisfying the small motion condition. At every time frame, the motion field was used to deform horizontally and vertically tagged synthetic volumes. Fig. 6(d) shows the x-y cross section of the simulated tagged volumes before and after deformation at one time frame. These volumes were processed with PVIRA, yielding a motion estimate shown in Fig. 6(b) and its magnitude of error from the truth shown in Fig. 6(e). For PVIRA, we chose the smoothing parameter in Step 7 as zero and that in Step 5 as $\sigma = 6$. This specific selection will be justified in a following experiment. The errors of internal voxels are all less than 0.2 mm. Fig. 6(c) shows the simultaneously generated inverse field and Fig. 6(f) is the magnitude of error when the inverse field was compared with PVIRA's motion estimate when the two input time frames' order was reversed (testing inverse-consistency). Fig. 6(g) shows the Jacobian determinant of this cross section (Jacobian $\approx$ 1 indicates incompressibility). All the above figures are shown at time frame 10 (max displacement 2.8 mm). Besides this particular frame, the estimation error from the truth of all 18 time frames are box-plotted in Fig. 6(h), where center bars indicate the median with a 25 and 75 percentile box. All medians are less than 0.1 voxel. The outliers are errors at the boundary such as the red spots in Fig. 6(e).

For comparison, 3D HARP, IDEA, and a direct iLogDemons intensity registration were also tested with the same simulation. 3D HARP required no parameter selection. For IDEA, since sparse dataset needed to be created first, we removed two slices out of each three slices from generated dense volumes to simulate a sparse acquisition resembling our experimental sparsity condition. For iLogDemons, we used the same smoothing parameters as PVIRA. All methods provided reasonable results visually similar to the truth. We computed the magnitude of error, composed inverse and forward motions to test inversion quality, tested inverse-consistency, and computed the Jacobian determinant of all four methods over all time frames. The resulting statistics are listed in Table I, including the average execution time for each time frame. The mean estimation error of IDEA was slightly higher than the other methods, but all were under 1/10 voxel. Note that for inverse motion, since PVIRA and iLogDemons automatically provided an inverse field, we used an extra step of a fixed point method [71] to numerically compute the inverse of 3D HARP and IDEA. This extra step was fast, taking 0.6 s/frm on average. The inversion errors are around the same level (Table I), but PVIRA and iLogDemons showed slightly better inverse-consistency. Lastly, although only 3D HARP is not an incompressible method, its Jacobian determinant was also close to 1 because the simulated rotation field was essentially incompressible and 3D HARP provided a close estimation. But its local incompressibility fluctuated, causing a larger standard deviation. This simulation demonstrated that both PVIRA and iLogDemons contain all the properties of HARP and IDEA while maintaining an accuracy close to both, and are much faster. All experiments are performed on an Intel Core i5 2.29GHz, 8 GB memory, and 64-bit Windows computer.

Since PVIRA and iLogDemons showed similar performance, in order to compare the use of phase to the use of

TABLE I: Brain Rotation Simulation Test Result (errors are in voxels and time is in seconds)

	HARP	IDEA	Intensity	PVIRA
Estimation Err	0.06 ± 0.06	0.08 ± 0.07	0.07 ± 0.07	0.07 ± 0.06
Inversion Err	0.11 ± 0.13	0.12 ± 0.13	0.13 ± 0.14	0.13 ± 0.14
Inv-consist Err	0.12 ± 0.09	0.15 ± 0.13	0.10 ± 0.05	0.10 ± 0.05
Jacobian	0.98 ± 0.14	1.00 ± 0.05	1.00 ± 0.03	1.01 ± 0.03
Time/frm	144	527	79	89

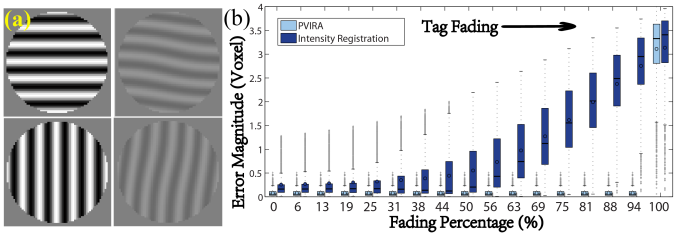

Fig. 7: Comparison of PVIRA and intensity registration. (a) Stationary tagged image and faded tags at 88%. (b) Box-plotted error magnitude under different tag fading levels. Center bar = median. Circle = mean.

intensity, we established a tag fading experiment to specifically test the two methods. We modified the previous simulation as follows. While the first time frame was kept stationary and undeformed, the remaining 17 time frames used the same amount of displacement (maximum rotation of 4.8 mm) from the above experiment. However, from time frame 2 to 17, the magnitude of the generated sinusoidal tag pattern linearly decreased from 1 to 0, yielding a sequence of deformed tagged images with low contrast. An example at time frame 15 with 88% tag fading was shown in Fig. 7(a). The estimation results from PVIRA and intensity iLogDemons were compared with the truth, and Fig. 7(b) shows the boxplotted error magnitudes at all tag fading levels. An immediate observation is that all PVIRA results are the same, because harmonic phase is not a property affected by tag fading. Unless the tags completely faded to zero (at the last frame) leaving no harmonic peak, the matching of phase by PVIRA kept the same good accuracy. However, iLogDemons was unable to match the faded intensity values to the correct position, yielding motion estimates with insufficient amount of magnitude and growing errors as tags continued to fade. In this scenario, the use of phase showed a clear advantage over intensity methods.

Next, we tested the effect of noise on motion estimation. Normally distributed Gaussian noise was added to the brain rotation simulation. We tested ten scenarios when the noise energy was raised step-wisely from 0.1 to 1.0 (by increasing Gaussian variance) so that the signal to noise ratio (SNR) decreased from 20 to 0 (see Fig. 8(b)). An example of tagged volumes at SNR = 8 and max displacement of 2.8 mm are shown in Fig. 8(a). The estimated motion fields from three phase-based methods (PVIRA, HARP, and IDEA) and direct intensity registration were compared with the truth, and results from both PVIRA and intensity registration were closer to the truth due to the contribution from their internal regularization.

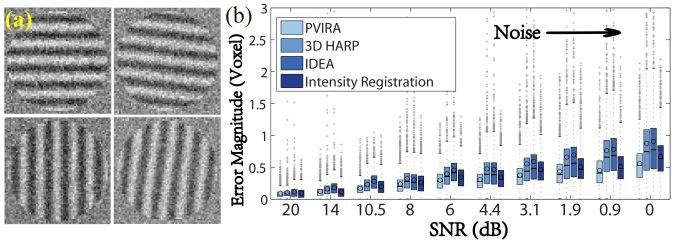

Fig. 8: Brain rotation simulation with noise. (a) Tagged images with noise (SNR = 8 and with 2.8 mm max displacement). (b) Box-plotted error magnitude under different noise levels. Center bar = median. Circle = mean.

The magnitude of error at all SNR levels is boxed-plotted in Fig. 8(b). Although the error increases rapidly as noise increases, PVIRA's error stays lower than the other three methods in all circumstances: both its mean and median are lower and it has fewer numbers of outliers. Note that iLogDemons also benefited from its regularization property and out-performed HARP and IDEA, but the inconsistent noisy intensities still affected its performance more than PVIRA. In this simulation, PVIRA is more robust to noise than all the other methods (a student t-test on all noise levels indicated $p < 0.01$).

Next, we studied parameter selection of the level of smoothness of PVIRA's regularization Gaussian kernel. The current algorithm does not contain an automatic parameter optimization mechanism, and therefore the smoothing parameters must be manually specified. Steps 5 and 7 of Algorithm 2 are two regularizations of PVIRA both implemented using Gaussian smoothing. Here we kept the smoothing in Step 7 as zero and examined the effect of changes in the Gaussian kernel variance in Step 5. We tested the ten previous SNR levels ranging from 0 to 20. With each SNR level, different regularization parameters were used with Gaussian kernel variance set to 0, 2, 4, 6, 8, 10, and 12—from zero to strong regularization. PVIRA was applied with all parameters and all noise levels and the mean estimation error was computed and plotted in Fig. 9. Since the generation of noise was random, in order to increase sample size, for each noise level the entire experiment was repeated twenty times, each with a new random noise, and Fig. 9 shows the mean of all repetitions. Apparently, when the noise level is high, the estimation error is reduced with stronger regularization ($\sigma = 12$). However, this also causes over-smoothing when the noise level is low, reducing accuracy in return. According to Fig. 9, a σ value of 6–8 is well-balanced, reducing error under high noise while keeping a lower error under low noise. In the experiments below we used $\sigma = 6$. We emphasize that keeping a zero smoothing parameter was only to simplify the selection experiment. However, from our observations in using PVIRA, either of the two parameters was able to achieve a proper level of smoothing. Therefore, making another parameter selection experiment for the other parameter is also justifiable.

All brain rotation simulations focused on the estimation of x-y motion and were homogeneous in the z direction. Therefore, we simulated tongue motions containing larger

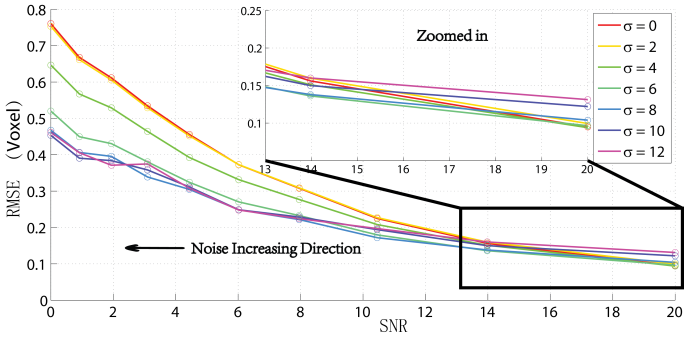

Fig. 9: PVIRA estimation error with different regularization and noise levels. σ is the standard deviation of the regularizing Gaussian kernel.

amount of displacements in all three directions. We simulated a forwardly-protruding tongue motion by interpolating nodal displacement results from a forward finite element simulation under muscular activation onto a $60 \times 40 \times 50$ grid in ten time frames. The model geometry was derived from the ArtiSynth biomechanical modeling toolkit [72], [73], and was solved using the FEBio software suite [74]. Material coefficients were manually adjusted to generate displacements similar to the magnitude expected in a live subject and to enforce incompressibility. We performed the same tests as in the brain simulation by using all four methods first and then computed their estimation error, inversion and consistency error, and Jacobian determinant. An example of one axial slice and one sagittal slice is shown in Fig. 10 with a 6.8 mm maximum displacement. In this simple motion when the tongue tip was protruding forward and downward, the tongue was using x and z motion to expand forward while using y motion to compress from left and right. Fig. 10(c) shows the result of three phase-based methods. Proper estimates were made within the body of the tongue, but 3D HARP and IDEA suffer from stronger boundary effects. In Fig. 10(b), all methods show strong boundary effects, and IDEA also shows more planar artifacts inside the tongue body because of its vector-spline interpolation process based on 2D motion estimation.

Table II lists the statistics of all four methods over all time frames. The extra fixed point step for 3D HARP and IDEA took 0.8 s/frm on average and was counted in. PVIRA is more accurate on average and has less variance than the other two phase-based methods. IDEA is less accurate due to the artifacts from sparse data. PVIRA also shows better inverse consistency and faster speed. Also, IDEA and PVIRA are both more incompressible than 3D HARP. Since this simulation had neither noise nor tag fading, intensity iLogDemons demonstrates a similar level of accuracy comparing to PVIRA.

B. Estimation of Brain Motion in Mild Accelerations

To characterize brain biomechanics in vivo during an angular acceleration, a controlled mild rotation was generated in each of three healthy volunteers. Each subject, lying down in a Siemens 3.0T mMR Biograph scanner (Siemens, Munich, Germany), was constrained with a head rotation device that accelerates the head towards the left shoulder [5]. In repeated

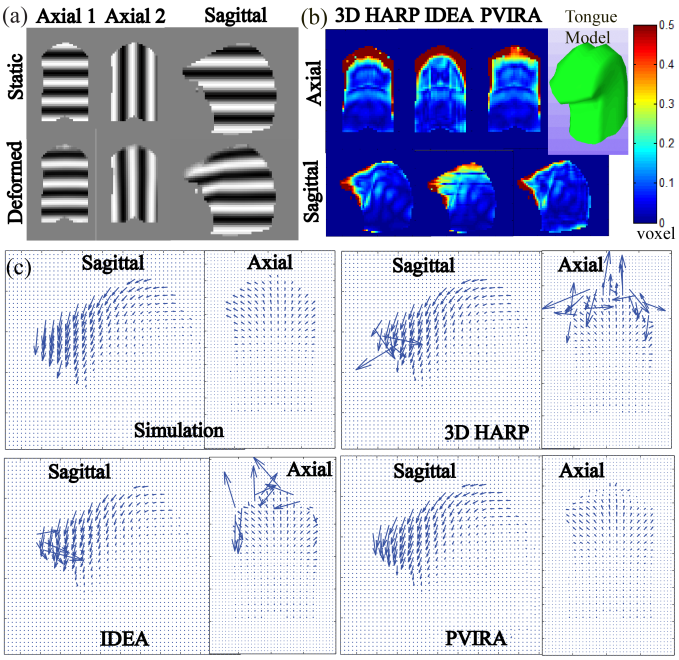

Fig. 10: Test of PVIRA on simulated tongue protrusion. (a) Tagged slices with three tag directions (max displacement 6.8 mm). (b) Estimation error of three phase-based methods. (c) Simulated motion and estimated motion from three phase-based methods.

TABLE II: Tongue Protrusion Simulation Test Result (errors are in voxels and time is in seconds)

	HARP	IDEA	Intensity	PVIRA
Estimation Err	0.19 ± 0.81	0.21 ± 0.69	0.12 ± 0.20	0.13 ± 0.17
Inversion Err	0.15 ± 0.26	0.14 ± 0.23	0.12 ± 0.10	0.12 ± 0.12
Inv-consist Err	0.15 ± 0.17	0.18 ± 0.20	0.10 ± 0.04	0.09 ± 0.03
Jacobian	1.05 ± 0.55	1.00 ± 0.11	1.00 ± 0.05	1.00 ± 0.07
Time/frm	112	627	102	107

motions, tagged images were acquired with a SPAMM pulse sequence into sparse parallel slices covering the brain region and spanning across 12 time frames (resolution: 1.5 mm in-plane and 8.00 mm through-plane). On axial slices, horizontal and vertical tags were used to capture left–right motion and anterior–posterior motion. Then the remaining superior–inferior motion was captured with horizontal tags on sagittal slices (see Fig. 11(g)). Considering the existence of noise and tag fading in real data, we only applied phase-based methods of 3D HARP, IDEA, and PVIRA to estimate 3D motion at every time frame. Two examples of a subject's motion estimate at time frame 3 (strongest left rotation) and time frame 7 (strongest right rotation) are shown in Figs. 11(a) to 11(f). Visually, the three estimates are similar. We also computed the Jacobian determinant to check incompressibility (see Fig. 11(i) for example). Since 3D HARP with phase tracking is closer to the actual HARP measurements except at the boundaries, when the true motion is unknown, to compare the performance between the two incompressible methods (PVIRA and IDEA), we used 3D HARP as a reference and computed the two

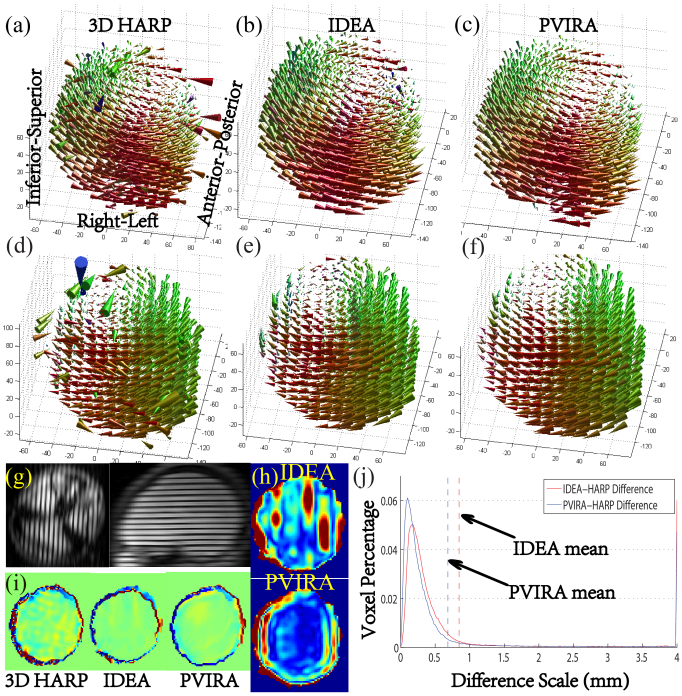

Fig. 11: Brain mild acceleration motion estimation. (a)–(c) Time frame for max counter-clockwise rotation. (d)–(f) Time frame for max clockwise rotation. (g) Tagged axial and sagittal slices. (h) Estimation difference from HARP. Colorbar ranges from 0 to 0.5 as in the previous figures. (i) Jacobian determinants. (j) Histogram of difference from HARP using IDEA and PVIRA. Note: *cones* are used to visualize motion fields where cone length indicates magnitude and cone color follows conventional diffusion imaging scheme (red = left–right, green = anterior–posterior, blue = superior–inferior).

TABLE III: Brain Acceleration Motion Estimation Results

	HARP	IDEA	PVIRA
HARP Difference (mm)	0	0.84 ± 1.80	0.62 ± 1.24
Jacobian Determinant	1.11 ± 0.82	1.01 ± 0.27	1.01 ± 0.26
Runtime per Frame (min)	4.9	141.6	4.7

methods' differences from it (see Fig. 11(h) for example). We plotted the normalized histogram of the two differences in Fig. 11(j). PVIRA had more voxels that had smaller difference and its mean difference was also smaller than that of IDEA. Especially, this was the case for all 33 volumes of the three human subjects. We conclude that PVIRA result is closer to HARP than IDEA (student t-test on all volumes indicated $p < 0.05$). The mean difference, Jacobian determinant, and average computing time for all 33 volumes are shown in Table III.

C. Estimation of Tongue Motion in Speech

To capture the tongue's deformation in speech, a controlled speech task was performed by two healthy subjects. In a Siemens 3.0T mMR Biograph scanner under a CSPAMM pulse sequence, the subjects repeatedly spoke a designed utterance "a souk" following a rhythm, where forward motion

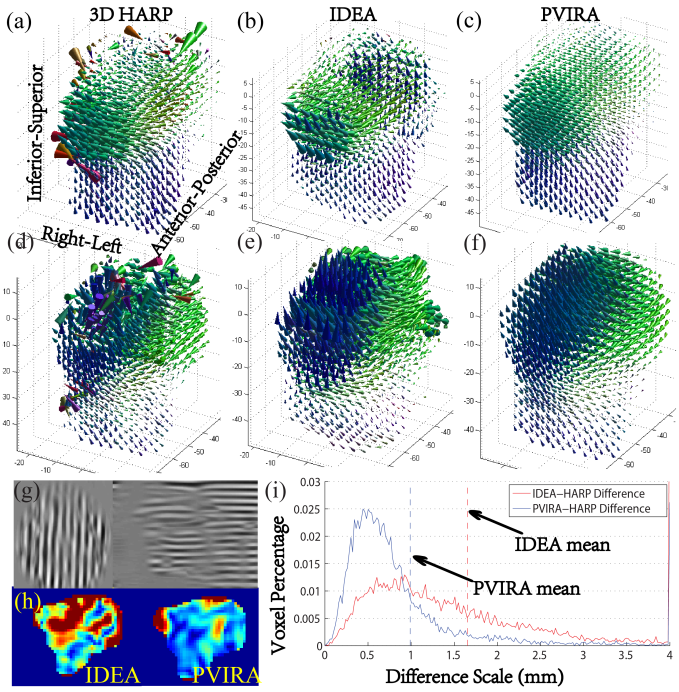

Fig. 12: Tongue motion estimation in speech. (a)–(c) Time frame for max forward motion. (d)–(f) Time frame for max upward motion. (g) Tagged axial and sagittal slices. (h) Estimation difference from HARP. Colorbar ranges from 0 to 0.5 as in the previous figures. (i) Histogram of difference from HARP using IDEA and PVIRA.

happened at time frames leading to /s/ and upward motion happened at time frames leading to /k/. The entire motion cycle happened within one second and 26 time frames were captured into tagged slices covering the tongue region [75]. The data resolution is 1.88 mm in-plane and 6.00 mm through-plane. On sagittal slices, horizontal and vertical tags were used to capture superior–inferior motion and anterior–posterior motion. Then the remaining left–right motion was captured with vertical tags on axial slices (see Fig. 12(g)). We used 3D HARP, IDEA, and PVIRA to estimate the motion at every time frame for the two subjects. Excluding time frame 1, a total of 50 volumes was evaluated. Two examples of a subject's motion estimate at time frame 8 (strongest forward motion) and time frame 18 (strongest upward motoin) are shown in Figs. 12(a) to 12(f). In the tongue motion, the boundary effect of 3D HARP was stronger than that of the brain. We also computed the difference from HARP using the other two methods (see Fig. 12(h) for example) and its histogram is plotted in Fig. 12(j). The PVIRA result is also closer to HARP than IDEA for all 50 volumes from two subjects (student t-test on all volumes indicated $p < 0.05$). The mean difference, Jacobian determinant, and average computing time for 50 volumes are shown in Table IV.

D. Cardiac Data Tracking Validation

Finally, we applied the four methods on an open cardiac dataset described in [62]. The volunteer data on myocardial

TABLE IV: Tongue Motion Estimation Results

	HARP	IDEA	PVIRA
HARP Difference (mm)	0	1.63 ± 1.70	0.97 ± 1.48
Jacobian Determinant	1.21 ± 1.83	1.00 ± 0.37	1.00 ± 0.21
Runtime per Frame (min)	0.3	9.1	0.3

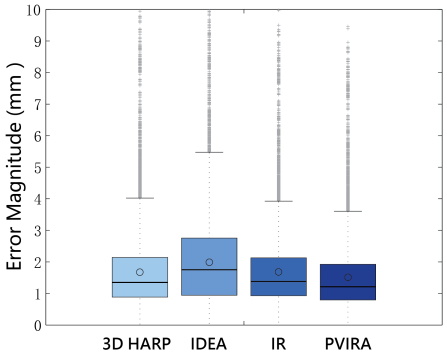

Fig. 13: Magnitude of volunteers' cardiac landmark tracking errors using HARP, IDEA, intensity registration, and PVIRA. Center bar = median. Circle = mean.

tissue tracking was used to evaluate the performance of 3D HARP, IDEA, intensity registration, and PVIRA. In the myocardium, 24 landmarks were manually tracked by each volunteer to be considered as reference. These landmarks were also tracked by the motion fields produced by each estimation method. Fig. 13 shows the boxplotted landmark tracking errors for all volunteers at all time frames. Both the mean and median of PVIRA are lower than the other methods. While IDEA has the largest error, intensity registration shows a similar level of performance to HARP, but has slightly higher error than PVIRA (student t-test indicated $p < 0.05$).

IV. Discussion

Without noise or tag fading, PVIRA demonstrated a similar degree of accuracy to 3D HARP, IDEA, and iLogDemons intensity registration. However, 3D HARP has no regularization or other physical constraints and should be considered a baseline method. Regarding IDEA, to achieve the same final estimation as other methods, 2D tracking, 3D super-resolution reconstruction, and 3D image segmentation are needed that require multiple preprocessing steps. In our experiments, these steps took on average about 3 hours per real subject. Also, to estimate inverse motion, numerical methods require extra processing steps and can cause numerical errors on the boundary. Furthermore, the execution time of IDEA was much slower than PVIRA due to its multi-step divergence-free vector spline process. Eventually, IDEA took days to process all subjects while PVIRA took hours. In noise simulations, PVIRA showed great robustness over the other two phase-based methods. Helped by its internal regularization, PVIRA results on the real data were also visually smoother. From Figs. 11(h) and 12(h), planar-shaped artifacts can be observed in IDEA estimation due to its use of sparse slices. However, PVIRA starts the estimation with a dense interpolation and does not suffer from these artifacts. This also explains the reason that PVIRA is closer to HARP than IDEA because both PVIRA and HARP are volume-based processing methods.

On the other hand, direct iLogDemons intensity registration showed a similar level of simplicity and accuracy to PVIRA in most cases. Moreover, it requires no phase computation or phase unwrapping manipulation and seems more straightforward. However, it can be affected greatly by tag fading and noise. Especially, the real data we used in our brain experiment and speech experiment showed a tag fading amount of around 90% in one second's acquisition time when comparing the last time frame to the first time frame. From Fig. 7, this level of tag fading can yield a mean error of around 2.5 voxels, while PVIRA stays unaffected at a less than 0.5 voxel error. Also, in real cases, since the tagged images we acquired typically have good SNR (greater than 20), from Fig. 8, we can see that both PVIRA and intensity methods are at their highest level of performance and not affected much. We can conclude that practically, considering the major impact of tag fading and potential effect of noise, phase methods are preferred over intensity methods.

Comparing to other phase-based methods, we also note two extra advantages of PVIRA that are not discussed in-depth in this work: 1) PVIRA has the capability to estimate motion on all tissue regions covered by tags instead of being restricted to the segmented region as is required by IDEA. This provides potential for advanced motion studies on neighboring tissues or organs. 2) PVIRA enables direct computation of motion between any two time frames. Especially, the so-called "running displacements" between two consecutive time frames can be particularly interesting to speech experts. However, since methods such as IDEA require its estimated motion to be with respect to the time frame when the tags are flat (i.e., time frame 1), direct running motion computation is not possible.

In most of the shown results, boundary effects are present. We first clarify they are mainly due to the use of previously available binary masks on the tissue of interest in all of our experiments. The reasons for applying such masks are 1) for better visualization and 2) to speed up all of our tests. On the other hand, in regions such as tissue-air boundary, PVIRA can indeed suffer from more boundary effects. A potential solution is to compute extra boundary deformations in a separate process and incorporate them into the estimation pipeline, as proposed in work [41]. Moreover, additional hidden parameters' optimization needs to be studied, e.g., the effect of two regularization steps can be further explored to prevent over-smoothing, and the impact of coarser or finer 3D tag interpolation resolutions can be studied to better balance accuracy and efficiency. Automatic parameter selection with prior knowledge could be a potential direction for improvement.

V. Conclusion

We proposed a novel phase-based method PVIRA to process tagged images for motion estimation. A new velocity update specifically designed to interpolate phase volumes was used, yielding an estimate that is dense, diffeomorphic, incompressible, and inverse-consistent. Compared with existing methods,

PVIRA demonstrated comparable accuracy, showed strong robustness against noise and tag fading, greatly simplified the processing work flow, and was much faster to execute. More importantly, PVIRA addresses the phase tracking problem in the context of incompressible registration, which has not been well-explored in majority of previous works.

REFERENCES

[1] E.H. Ibrahim, "Myocardial tagging by cardiovascular magnetic resonance: evolution of techniques–pulse sequences, analysis algorithms, and applications," *J. Cardiovasc Magn. Reson.*, vol. 13, pp. 36, 2011.

[2] A. Kolipaka, G.P. Chatzimavroudis, R.D. White, M.L. Lieber, and R.M. Setser, "Relationship between the extent of non-viable myocardium and regional left ventricular function in chronic ischemic heart disease," *Journal of Cardiovascular Magnetic Resonance*, vol. 7, no. 3, pp. 573–579, 2005.

[3] V. Parthasarathy, J. L. Prince, M. Stone, E. Murano, and M. NessAiver, "Measuring tongue motion from tagged Cine-MR using harmonic phase (HARP) processing," *J. Acoustic Society of America*, vol. 121, no. 1, pp. 491–504, 2007.

[4] A.A. Sabet, E. Christoforou, B. Zatlin, G.M. Genin, and P.V. Bayly, "Deformation of the human brain induced by mild angular head acceleration," *J. Biomech*, vol. 41, no. 2, pp. 307–315, 2008.

[5] A.K. Knutsen, E. Magrath, J.E. McEntee, F. Xing, J.L. Prince, P.V. Bayly, J.A. Butman, and D.L. Pham, "Improved measurement of brain deformation during mild head acceleration using a novel tagged MRI sequence," *Journal of Biomechanics*, vol. 47, no. 14, pp. 3475–3481, 2014.

[6] E.A. Zerhouni, D.M. Parish, W.J. Rogers, A. Yang, and E.P. Shapiro, "Human heart: tagging with MR imaging–a method for noninvasive assessment of myocardial motion," *Radiology*, vol. 169, no. 1, pp. 59–63, 1988.

[7] L. Axel and L. Dougherty, "MR imaging of motion with spatial modulation of magnetization," *Radiology*, vol. 171, no. 3, pp. 841–845, 1989.

[8] M.A. Guttman, J.L. Prince, and E.R. McVeigh, "Tag and contour detection in tagged MR images of the left ventricle," *Medical Imaging, IEEE Transactions on*, vol. 13, no. 1, pp. 74–88, 1994.

[9] M.A. Guttman, E. Zerhouni, E.R. McVeigh, et al., "Analysis of cardiac function from MR images," *Computer Graphics and Applications, IEEE*, vol. 17, no. 1, pp. 30–38, 1997.

[10] A. Young, D.L. Kraitchman, L. Dougherty, L. Axel, et al., "Tracking and finite element analysis of stripe deformation in magnetic resonance tagging," *Medical Imaging, IEEE Transactions on*, vol. 14, no. 3, pp. 413–421, 1995.

[11] A. Amini, Y. Chen, R.W. Curwen, V. Mani, J. Sun, et al., "Coupled B-snake grids and constrained thin-plate splines for analysis of 2-D tissue deformations from tagged MRI," *Medical Imaging, IEEE Transactions on*, vol. 17, no. 3, pp. 344–356, 1998.

[12] W.S. Kerwin and J.L. Prince, "Cardiac material markers from tagged MR images," *Medical Image Analysis*, vol. 2, no. 4, pp. 339–353, 1998.

[13] N.F. Osman, W.S. Kerwin, E.R. McVeigh, and J.L. Prince, "Cardiac motion tracking using CINE harmonic phase (HARP) magnetic resonance imaging," *Magnetic Resonance Medicine*, vol. 42, pp. 1048–1060, 1999.

[14] N.F. Osman, E.R. McVeigh, and J.L. Prince, "Imaging heart motion using harmonic phase MRI," *Medical Imaging, IEEE Transactions on*, vol. 19, no. 3, pp. 186–202, 2000.

[15] N.F. Osman and J.L. Prince, "Visualizing myocardial function using HARP MRI," *Physics in medicine and biology*, vol. 45, no. 6, pp. 1665, 2000.

[16] T. Chen, X. Wang, S. Chung, D. Metaxas, and L. Axel, "Automated 3D motion tracking using gabor filter bank, robust point matching, and deformable models," *Medical Imaging, IEEE Transactions on*, vol. 29, no. 1, pp. 1–11, 2010.

[17] S. Ryf, M.A. Spiegel, M. Gerber, and P. Boesiger, "Myocardial tagging with 3D-CSPAMM," *J. Magnetic Resonance Imaging*, vol. 16, pp. 320–325, 2002.

[18] T.G. Reese, D.A. Feinberg, J. Dou, and V.J. Wedeen, "Phase contrast MRI of myocardial 3D strain by encoding contiguous slices in a single shot," *Magnetic resonance in medicine*, vol. 47, no. 4, pp. 665–676, 2002.

[19] K.Z. Abd-Elmoniem, N.F. Osman, J.L. Prince, and M. Stuber, "Three-dimensional magnetic resonance myocardial motion tracking from a single image plane," *Magnetic Resonance in Medicine*, vol. 58, no. 1, pp. 92–102, 2007.

[20] B.S. Spottiswoode, X. Zhong, C.H. Lorenz, B.M. Mayosi, E.M. Meintjes, and F.H. Epstein, "3D myocardial tissue tracking with slice followed cine DENSE MRI," *Journal of Magnetic Resonance Imaging*, vol. 27, no. 5, pp. 1019–1027, 2008.

[21] F. Yin, C. Chan, and R.M. Judd, "Compressibility of perfused passive myocardium," *American Journal of Physiology-Heart and Circulatory Physiology*, vol. 271, no. 5, pp. H1864–H1870, 1996.

[22] I. Rodriguez, D.B. Ennis, and H. Wen, "Noninvasive measurement of myocardial tissue volume change during systolic contraction and diastolic relaxation in the canine left ventricle," *Magnetic resonance in medicine*, vol. 55, no. 3, pp. 484–490, 2006.

[23] R.J. Gilbert, V.J. Napadow, T.A. Gaige, and V.J. Wedeen, "Anatomical basis of lingual hydrostatic deformation," *Journal of Experimental Biology*, vol. 210, no. 23, pp. 4069–4082, 2007.

[24] W.M. Kier and K.K. Smith, "Tongues, tentacles and trunks: the biomechanics of movement in muscular-hydrostats," *Zoological Journal of the Linnean Society*, vol. 83, no. 4, pp. 307–324, 1985.

[25] W.G. O'Dell, C.C. Moore, W.C. Hunter, E.A. Zerhouni, and E.R. McVeigh, "Three-dimensional myocardial deformations: calculation with displacement field fitting to tagged MR images," *Radiology*, vol. 195, no. 3, pp. 829–835, Jun 1995.

[26] M. Li, H. Gupta, S.G. Lloyd, L.J. DellItalia, and T.S. Denney Jr, "A graph theoretic approach for computing 3D+ time biventricular cardiac strain from tagged MRI data," *Medical image analysis*, vol. 35, pp. 46–57, 2017.

[27] T.S. Denney and J.L. Prince, "Reconstruction of 3-D left ventricular motion from planar tagged cardiac MR images: an estimation theoretic approach," *Medical Imaging, IEEE Transactions on*, vol. 14, no. 4, pp. 625–635, 1995.

[28] I. Haber, D.N. Metaxas, and L. Axel, "Three-dimensional motion reconstruction and analysis of the right ventricle using tagged MRI," *Medical Image Analysis*, vol. 4, no. 4, pp. 335–355, 2000.

[29] J. Huang, D. Abendschein, V.G. Davila-Roman, and A. Amini, "Spatio-temporal tracking of myocardial deformations with a 4-D B-spline model from tagged MRI," *Medical Imaging, IEEE Transactions on*, vol. 18, no. 10, pp. 957–972, 1999.

[30] C. Ozturk and E.R. McVeigh, "Four-dimensional B-spline based motion analysis of tagged MR images: introduction and in vivo validation," *Physics in medicine and biology*, vol. 45, no. 6, pp. 1683, 2000.

[31] X. Liu, K.Z. Abd-Elmoniem, M. Stone, E.Z. Murano, J. Zhuo, R.P. Gullapalli, and J.L. Prince, "Incompressible deformation estimation algorithm (IDEA) from tagged MR images," *Medical Imaging, IEEE Transactions on*, vol. 31, no. 2, pp. 326–340, 2012.

[32] H. Liu, M. Yan, E. Song, J. Wang, Q. Wang, R. Jin, L. Jin, and C. Hung, "Myocardial motion estimation of tagged cardiac magnetic resonance images using tag motion constraints and multi-level b-splines interpolation," *Magnetic resonance imaging*, vol. 34, no. 4, pp. 579–595, 2016.

[33] P. Shi, A.J. Sinusas, R.T. Constable, and J.S. Duncan, "Volumetric deformation analysis using mechanics-based data fusion: Applications in cardiac motion recovery," *International Journal of Computer Vision*, vol. 35, no. 1, pp. 87–107, 1999.

[34] X. Papademetris, A.J. Sinusas, D.P. Dione, R.T. Constable, and J.S. Duncan, "Estimation of 3-D left ventricular deformation from medical images using biomechanical models," *Medical Imaging, IEEE Transactions on*, vol. 21, no. 7, pp. 786–800, 2002.

[35] Y. Zhou, O. Bernard, E. Saloux, A. Manrique, P. Allain, S. Makram-Ebeid, and M. De Craene, "3D harmonic phase tracking with anatomical regularization," *Medical Image Analysis*, vol. 26, no. 1, pp. 70–81, 2015.

[36] A.A. Amini and J.L. Prince, *Measurement of cardiac deformations from MRI: Physical and mathematical models*, vol. 23, Springer Science & Business Media, 2013.

[37] J. Lee, J. Woo, F. Xing, E.Z. Murano, M. Stone, and J.L. Prince, "Semi-automatic segmentation for 3D motion analysis of the tongue with dynamic MRI," *Computerized Medical Imaging and Graphics*, vol. 38, no. 8, pp. 714–724, 2014.

[38] D.L. Pham, C. Xu, and J.L. Prince, "Current methods in medical image segmentation 1," *Annual review of biomedical engineering*, vol. 2, no. 1, pp. 315–337, 2000.

[39] A. Bistoquet, J. Oshinski, and O. Skrinjar, "Left ventricular deformation recovery from cine MRI using an incompressible model," *Medical Imaging, IEEE Transactions on*, vol. 26, no. 9, pp. 1136–1153, 2007.

[40] A. Bistoquet, J. Oshinski, and O. Skrinjar, "Myocardial deformation recovery from cine MRI using a nearly incompressible biventricular model," *Medical image analysis*, vol. 12, no. 1, pp. 69–85, 2008.

[41] F. Xing, J. Woo, E.Z. Murano, J. Lee, M. Stone, and J.L. Prince, "3D tongue motion from tagged and cine MR images," in *Medical Image Computing and Computer-Assisted Intervention–MICCAI 2013*, pp. 41–48. Springer, 2013.

[42] C. Petitjean, N. Rougon, F. Prêteux, P. Cluzel, and P. Grenier, "Measuring myocardial deformations in tagged MR image sequences using informational non-rigid registration," in *International Workshop on Functional Imaging and Modeling of the Heart*. Springer, 2003, pp. 162–172.

[43] D. Perperidis, R.H. Mohiaddin, and D. Rueckert, "Spatio-temporal free-form registration of cardiac MR image sequences," *Medical image analysis*, vol. 9, no. 5, pp. 441–456, 2005.

[44] M.J. Ledesma-Carbayo, A. Bajo, C. Santa Marta, E. Perez-David, M.A. Garcia-Fernandez, M. Desco, and A. Santos, "Fully automatic cardiac motion estimation from tagged MRI using non-rigid registration techniques," in *Computers in Cardiology, 2006*. IEEE, 2006, pp. 305–308.

[45] N.J. Tustison and A.A. Amini, "Biventricular myocardial strains via nonrigid registration of AnFigatomical NURBS models," *IEEE Transactions on Medical Imaging*, vol. 25, no. 1, pp. 94–112, 2006.

[46] M.J. Ledesma-Carbayo, J.A. Derbyshire, S. Sampath, A. Santos, M. Desco, and E.R. McVeigh, "Unsupervised estimation of myocardial displacement from tagged MR sequences using nonrigid registration," *Magnetic Resonance in Medicine*, vol. 59, no. 1, pp. 181–189, 2008.

[47] E. Oubel, M. De Craene, A.O. Hero, A. Pourmorteza, M. Huguet, G. Avegliano, B.H. Bijnens, and A.F. Frangi, "Cardiac motion estimation by joint alignment of tagged MRI sequences," *Medical image analysis*, vol. 16, no. 1, pp. 339–350, 2012.

[48] N.F. Rougon, C. Petitjean, and F.J. Preteux, "Building and using a statistical 3D motion atlas for analyzing myocardial contraction in MRI," in *Medical Imaging 2004*. International Society for Optics and Photonics, 2004, pp. 253–264.

[49] R. Chandrashekara, R.H. Mohiaddin, and D. Rueckert, "Analysis of 3-D myocardial motion in tagged MR images using nonrigid image registration," *IEEE Transactions on Medical Imaging*, vol. 23, no. 10, pp. 1245–1250, 2004.

[50] R. Chandrashekara, R. Mohiaddin, R.S. Razavi, and D. Rueckert, "Nonrigid image registration with subdivision lattices: Application to cardiac MR image analysis," in *International Conference on Medical Image Computing and Computer-Assisted Intervention*. Springer, 2007, pp. 335–342.

[51] M. De Craene, C. Tobon-Gomez, C. Butakoff, N. Duchateau, G. Piella, K.S. Rhode, and A.F. Frangi, "Temporal diffeomorphic free form deformation (TDFFD) applied to motion and deformation quantification of tagged MRI sequences," in *International Workshop on Statistical Atlases and Computational Models of the Heart*. Springer, 2011, pp. 68–77.

[52] M. De Craene, G. Piella, O. Camara, N. Duchateau, E. Silva, A. Doltra, J. Dhooge, J. Brugada, M. Sitges, and A.F. Frangi, "Temporal diffeomorphic free-form deformation: Application to motion and strain estimation from 3D echocardiography," *Medical Image Analysis*, vol. 16, no. 2, pp. 427–450, 2012.

[53] W. Shi, X. Zhuang, H. Wang, S. Duckett, D.V.N. Luong, C. Tobon-Gomez, K. Tung, P.J. Edwards, K.S. Rhode, R.S. Razavi, et al., "A comprehensive cardiac motion estimation framework using both untagged and 3-D tagged MR images based on nonrigid registration," *IEEE transactions on medical imaging*, vol. 31, no. 6, pp. 1263–1275, 2012.

[54] Y. Yu, S. Zhang, K. Li, D. Metaxas, and L. Axel, "Deformable models with sparsity constraints for cardiac motion analysis," *Medical image analysis*, vol. 18, no. 6, pp. 927–937, 2014.

[55] K. McLeod, A. Prakosa, T. Mansi, M. Sermesant, and X. Pennec, "An incompressible log-domain demons algorithm for tracking heart tissue," in *International Workshop on Statistical Atlases and Computational Models of the Heart*. Springer, 2011, pp. 55–67.

[56] T. Vercauteren, X. Pennec, A. Perchant, and N. Ayache, "Diffeomorphic demons: efficient non-parametric image registration," *NeuroImage*, vol. 45, no. 1, pp. S61–S72, 2009.

[57] T. Mansi, J.-M. Peyrat, M. Sermesant, H. Delingette, J. Blanc, Y. Boudjemline, and N. Ayache, "Physically-constrained diffeomorphic demons for the estimation of 3D myocardium strain from cine-MRI," in *Functional Imaging and Modeling of the Heart*, pp. 201–210. Springer, 2009.

[58] T. Mansi, X. Pennec, M. Sermesant, H. Delingette, and N. Ayache, "ilogdemons: A demons-based registration algorithm for tracking incompressible elastic biological tissues," *International journal of computer vision*, vol. 92, no. 1, pp. 92–111, 2011.

[59] T. Gautama and M.A. Van Hulle, "A phase-based approach to the estimation of the optical flow field using spatial filtering," *IEEE Transactions on Neural Networks*, vol. 13, no. 5, pp. 1127–1136, 2002.

[60] J.L. Prince and E.R. McVeigh, "Motion estimation from tagged MR image sequences," *Medical Imaging, IEEE Transactions on*, vol. 11, no. 2, pp. 238–249, 1992.

[61] Y. Zhou, M. De Craene, and O. Bernard, "Phase-based registration of cardiac tagged MR images using anatomical deformation model," in *Biomedical Imaging (ISBI), 2016 IEEE 13th International Symposium on*. IEEE, 2016, pp. 617–620.

[62] C. Tobon-Gomez, M. De Craene, K. Mcleod, L. Tautz, W. Shi, A. Hennemuth, A. Prakosa, H.i Wang, G. Carr-White, S. Kapetanakis, et al., "Benchmarking framework for myocardial tracking and deformation algorithms: An open access database," *Medical image analysis*, vol. 17, no. 6, pp. 632–648, 2013.

[63] T.M. Lehmann, C. Gönner, and K. Spitzer, "Survey: Interpolation methods in medical image processing," *Medical Imaging, IEEE Transactions on*, vol. 18, no. 11, pp. 1049–1075, 1999.

[64] M. Unser, A. Aldroubi, and M. Eden, "B-spline signal processing. I. Theory," *Signal Processing, IEEE Transactions on*, vol. 41, no. 2, pp. 821–833, 1993.

[65] S. Nithiananthan, K.K. Brock, M.J. Daly, H. Chan, J.C. Irish, and J.H. Siewerdsen, "Demons deformable registration for CBCT-guided procedures in the head and neck: convergence and accuracy," *Medical Physics*, vol. 36, no. 10, pp. 4755–4764, 2009.

[66] H. Takajo and T. Takahashi, "Least-squares phase estimation from the phase difference," *JOSA A*, vol. 5, no. 3, pp. 416–425, 1988.

[67] D.C. Ghiglia and L.A. Romero, "Direct phase estimation from phase differences using fast elliptic partial differential equation solvers," *Optics letters*, vol. 14, no. 20, pp. 1107–1109, 1989.

[68] D.C. Ghiglia and M.D. Pritt, *Two-dimensional phase unwrapping: theory, algorithms, and software*, vol. 4.

[69] M. Jenkinson, "Fast, automated, N-dimensional phase-unwrapping algorithm," *Magnetic resonance in medicine*, vol. 49, no. 1, pp. 193–197, 2003.

[70] J.-M. Peyrat, H. Delingette, M. Sermesant, C. Xu, and N. Ayache, "Registration of 4D cardiac CT sequences under trajectory constraints with multichannel diffeomorphic demons," *Medical Imaging, IEEE Transactions on*, vol. 29, no. 7, pp. 1351–1368, 2010.

[71] M. Chen, W. Lu, Q. Chen, K.J. Ruchala, and G.H. Olivera, "A simple fixed-point approach to invert a deformation field," *Medical physics*, vol. 35, no. 1, pp. 81–88, 2007.

[72] J.E. Lloyd, I. Stavness, and S. Fels, "ArtiSynth: a fast interactive biomechanical modeling toolkit combining multibody and finite element simulation," in *Soft tissue biomechanical modeling for computer assisted surgery*, pp. 355–394. Springer, 2012.

[73] S. Fujita, J. Dang, N. Suzuki, and K. Honda, "A computational tongue model and its clinical application," *Oral Science International*, vol. 4, no. 2, pp. 97–109, 2007.

[74] S.A. Maas, B.J. Ellis, G.A. Ateshian, and J.A. Weiss, "FEBio: finite elements for biomechanics," *Journal of biomechanical engineering*, vol. 134, no. 1, pp. 011005, 2012.

[75] F. Xing, J. Woo, J. Lee, E.Z. Murano, M. Stone, and J.L. Prince, "Analysis of 3D tongue motion from tagged and cine MR images," in *Journal of Speech, Language, and Hearing Research*. 2016, in press.